Characterization of juvenile pyroclasts from the Kos Plateau Tuff (Aegean Arc): insights into the eruptive dynamics of a large rhyolitic eruption

Caroline Bouvet de Maisonneuve, Olivier Bachmann, Alain Burgisser

Characterization of juvenile pyroclasts from the Kos Plateau Tuff (Aegean Arc): insights into the eruptive dynamics of a large rhyolitic eruption

Caroline Bouvet de Maisonneuve[1,*], Olivier Bachmann[1,2], Alain Burgisser[3]

[1]Section des Sciences de la Terre, Université de Genève, 13 rue des maraîchers, 1205 Genève

[2]Department of Earth and Space Sciences, University of Washington, Mailstop 351310, Seattle, WA 98195-1310

[3]Institut des Sciences de la Terre d'Orléans, CNRS - Université d'Orléans, 1A, rue de la Férollerie, 45071 ORLEANS Cedex 2, France

[*]Corresponding author

Email addresses: Caroline.Bouvet@terre.unige.ch, bachmano@u.washington.edu, burgisse@cnrs-orleans.fr

Tel. No: +41223796627, Fax No: +41223793210

Manuscript for: *Bulletin of Volcanology*

Version: July 2, 2008

Word count: ~6900

Abstract

Silicic pumices formed during explosive volcanic eruptions are faithful recorders of the state of the magma in the conduit, close to or at the fragmentation level. We have characterized four types of pumices from the non-welded rhyolitic Kos Plateau Tuff, which erupted 161,000 years ago in the East Aegean Arc, Greece. The dominant type of pumice (>90 vol%) shows highly elongated tubular vesicles. These tube pumices occur throughout the eruption. Less common pumice types include: (1) “frothy” pumice (highly porous with large, sub-rounded vesicles), which form 5-10 vol% of the coarsest pyroclastic flow deposits, (2) dominantly “microvesicular” and systematically crystal-poor pumices, which are found in early erupted, fine-grained pyroclastic flow units, and are characterized by many small (<50 microns diam.) vesicles and few mm-sized, irregular voids, (3) grey or banded pumices, indicating the interaction between the rhyolite and a more mafic magma, which are found throughout the eruption sequence and display highly irregular bubble shapes. Except for the grey-banded pumices, all three other types are compositionally identical and were generated synchronously as they are found in the same pyroclastic units. They, therefore, record different conditions in the volcanic conduit leading to variable bubble nucleation, growth and coalescence. A total of 74 pumice samples have been characterized using thin section observation, SEM imagery, porosimetry, and permeametry. We show that the four pumice types have distinct total and connected porosity, tortuosity and permeability. Grey-banded pumices show large variations in petrophysical characteristics as a response to mingling of two different magmas. The microvesicular, crystal-poor, pumices have a bimodal bubble size distribution, interpreted as reflecting an early heterogeneous bubble nucleation event followed by homogeneous bubble nucleation close to fragmentation. Finally, the significant differences in porosity, tortuosity and

permeability in compositionally identical tube and frothy pumices are the result of variable shear rates in different parts of the conduit. Differential shear rates may be the result of either: (1) pure shear, inducing a vertical progression from frothy to tube and implying a relatively thick fragmentation zone to produce both types of pumices at the same time or (2) localized simple shear, inducing strongly tubular vesicles along the wall and near-spherical bubbles in the centre of the conduit and not necessarily requiring a thick fragmentation zone.

Keywords: Permeability, inertial effects, porosity, crystallinity, high-silica rhyolite, tortuosity, degassing.

1 Introduction

The efficiency of volatile escape from ascending magma in volcanic conduits is believed to play an important role in eruption dynamics, particularly in controlling shifts between explosive and effusive eruptive styles (Eichelberger et al. 1986; Jaupart and Allègre 1991; Woods and Koyaguchi 1994; Jaupart 1998). Transitions in eruptive style can occur in either direction, and be quite sudden, making volcanic risk very difficult to evaluate (Melnik 2000). Gas loss from a permeable magmatic foam is increasingly considered in eruption models (Papale 2001; Slezin 2003; Melnik et al. 2005), as it affects viscosity of the magma, density variation and pressure distribution in the magma column, and ultimately the location and style of magma fragmentation. Quantification of permeability development during magma ascent in conduits is therefore critical to the implementation of accurate eruption models, which are highly sensitive to the sharp decreases in bulk viscosity and density that accompany vesiculation. Permeability studies are more and more common (Eichelberger et al. 1986; Klug and Cashman 1996; Saar and Manga 1999; Jouniaux et al. 2000; Klug et al. 2002; Melnik and Sparks 2002; Rust and Cashman

2004; Mueller et al. 2005), although those accounting for inertial effects during permeability measurements are restricted to the most recent publications (Rust and Cashman 2004; Mueller et al. 2005; Wright et al. 2006). This study extends the database with 74 porosity and permeability measurements on non-welded, highly vesicular juvenile pyroclasts (pumice) from the Kos Plateau Tuff (KPT), a young, large-volume (>60 km^3; Allen 2001) rhyolitic ignimbrite from the Aegean arc.

The KPT deposit is of interest for such a study as; (1) it is young, well preserved and non welded, (2) it contains numerous large pumice clasts (divided into 4 types), and (3) the magma was viscous enough (high-SiO_2 rhyolite melt) to limit post-fragmentation bubble growth or collapse to a minimum (Thomas et al. 1994). Pumice clasts should therefore be representative samples of the magmatic foam immediately prior to fragmentation. The aim of the study is to make a detailed description of the pumice's petrophysical characteristics (quantification of crystal and vesicle content, degree of interconnectivity, vesicle morphology and permeability) in order to shed some light on conduit dynamics of large explosive rhyolitic eruptions. The KPT deposits give us the opportunity to compare pyroclasts with different petrophysical characteristics that developed during a same eruption.

2 Samples

2.1 Eruption and associated deposits

The KPT eruption, dated at 161 ka by $^{40}Ar/^{39}Ar$ on sanidine (Smith et al. 1996), is one of the major Quaternary explosive eruptions of the Mediterranean region. It generated at least 60 km^3 of rhyolitic pumice and ash that were deposited in the eastern Mediterranean area, with ash spreading up to 2000 km from the vent (Allen 2001). The deposits are exposed on the islands of

Tilos, Kalymnos, and Pachia as well as on the Bodrum and Datça peninsulas, but they are best preserved on Kos (Fig. 1). Due to their large volume and exceptional preservation, the KPT deposits have been intensively studied and well characterized (Allen and Cas 1998a, Allen and Cas 1998b, Allen et al. 1999 and Allen 2001). The next paragraph is a short summary of the work that has been done by Allen and Cas (1998a and 1998b), Allen et al. (1999) and Allen (2001).

Six units were defined, and there is no evidence for any significant time breaks between them (Fig. 2). **Unit A**, the stratigraphically lowest unit, is widespread, mainly to the southeast of Kos. The high fragmentation index (i.e. high ash/pumice ratio) and the presence of ash-coated lapilli contribute to the interpretation of Unit A as a phreatoplinian fallout deposit. **Unit B** is only exposed on central Kos and is lower in volume. As in unit A, lapillis are finely ash-coated suggesting that the material was deposited from a current moderately dilute (i.e., transitional between a surge and a pyroclastic flow) generated by the (partial?) collapse of the phreatoplinian eruption column. **Unit C** is exposed on central Kos and Pachia and has a relatively small volume. The eruptive conditions were transitional between an oscillating fountain and a more voluminous outpouring process. **Unit D** is a sequence of three non-welded ignimbrites, wherein the average grain size increases in each successive ignimbrite. They are widespread and their distribution is topographically controlled. Unit D has a moderate volume of about 10 km^3 DRE. **Unit E,** the largest (>25 km^3 DRE) of the KPT units, is a sequence of two ignimbrites which do not show much topographic control. On Kos, the lower ignimbrite overlies a strongly erosional contact and can include an extremely coarse (lithic clasts 1-2 m diameter) and thick (up to 3 m thick) basal lithic breccia named **Ebx** (Allen and Cas 1998b). The average grain size decreases upwards with successive ignimbrites, Ebx is interpreted to record eruption climax (Fig. 2). This unit is assigned

to a high velocity pyroclastic density current generated during the collapse of a caldera. **Unit F** is relatively voluminous (~7 km^3 DRE), but is rarely well preserved. There was no time break between the deposition of Units E and F, therefore Unit F has been interpreted as the product of an unsteady pyroclastic density current and the settling of the co-ignimbrite ash cloud.

2.2 Pumice clasts

Pumices are abundant in the deposits and can reach large sizes (up to a meter in diameter in unit E). They are typically rhyolitic in whole-rock composition (~76 ± 1 wt% SiO_2; Allen 1998) and contain plagioclase, sanidine, quartz, biotite, Fe-Ti oxides, zircon, apatite and monazite. On the basis of our recent observations, we have rearranged the pumice classification scheme of Allen (2001). We distinguish four types of pumices that we have named according to their most dominant macroscopic characteristic; tube pumices (~type II in Allen, 2001), frothy pumices (~type III and IV), microvesicular pumices (~type I) and grey-banded pumices (~type V). Scanned thin sections are shown in Fig. 3. A qualitative macroscopical description is given below:

a. **Tube pumices** have stretched to very stretched vesicles. They are white and phenocryst-rich. They occur in every unit of the KPT. The pumices analysed were about 8-14 cm in diameter.
b. **Frothy pumices** have large spherical vesicles. Like the tube pumices, they are white and phenocryst-rich. They only occur in the coarse pyroclastic flow units (D and E). Between pumices, a gradual transition from tube-shaped vesicles to spherical vesicles exists. In order to describe the two end-members, we avoided sampling pumices with intermediate characteristics. The pumices analysed were about 5-10 cm in diameter.

c. **Microvesicular pumices** are white to grey and systematically phenocryst-poor. They mostly contain small vesicles (<50 microns diam.), although some large, irregular cavities (5-8 mm in diameter; Fig. 3c) are present. They occur in Units A and B, and are generally small or intensely fractured. Pumices of this type are generally small, but two examples (that we analysed) were approx. 10 cm and 30 cm in diameter.

d. **Grey-banded pumices** (Fig. 3d) indicate the interaction of the resident rhyolitic magma with andesitic magma (Stadlbauer 1988; Allen 2001). They have small sub-spherical vesicles, and a few large vesicles that are highly irregular in shape. The dark bands contain some hornblende, clinopyroxene, and minor orthopyroxene. They are most common in unit E, but can also be found in the previous sub-units. The pumices analysed were about 5-10 cm in diameter.

Frothy, tube, and microvesicular pumices have the same mineralogy and rhyolitic composition (Allen 2001), but the microvesicular ones are crystal-poor while frothy and tube pumices are crystal-rich (Table 1). Grey-banded pumices are slightly less evolved in composition (a few percent lower in SiO_2 content), and contain hornblende and pyroxene, which are not present in the other pumice types. The presence of crystal-rich tube pumices alongside with crystal-poor, microvesicular pumices in the same deposits indicate that a crystal-rich and crystal-poor batch of rhyolitic magma were stored in the same reservoir. Grey-banded pumices record the interaction of the resident rhyolitic magma with a more mafic component. The hybridisation between the two magma types may have occurred in the magma chamber or during ascent in the conduit.

The eruption started (Units A and B of Allen, 2001) by evacuating both the crystal-poor material (see Fig. 10 of Allen, 2001) and some crystal-rich material (tube pumices) with a small

fraction of hybrid magma (grey-banded pumices). Starting from Unit C, microvesicular pumices were no longer erupted, suggesting that the eruptible crystal-poor magma was entirely drained by Units A and B or no longer sampled by the eruption. The eruption rate then intensified during the eruption of Units D and E. Although tube pumices are the most abundant type in Units D and E, frothy pumices appear at this level and are locally abundant (up to 10 vol% of the pumice fraction larger than 16 mm in diameter). Grey-banded pumices are also present in these units. Unit F contains only tube pumices.

Tube pumices were sampled in Units B to E on the islands of Kos, Kalymnos, and Tilos; frothy pumices were mainly sampled in Unit E on Kalymnos; grey-banded pumices were sampled in Units B and E on Kos and Kalymnos; and microvesicular pumices were sampled in Unit B on Kos (Fig. 1). No pumices from Units A or F were studied, as they are too small to be cored.

3 Analytical Methods

3.1 Crystallinity

Two different methods were used to estimate the amount of crystals:

(1) Image analysis using JMicroVision (Roduit 2006). Pumice clasts were embedded in glue before sawing to avoid breaking, and extra large thin sections (4 by 6 cm) were cut in order to sample a large surface area. The glue was died blue to allow the software to distinguish voids from white minerals. Using RGB (Red, Green, Blue) or HIS (Hue, Intensity, Saturation) channels, it was possible to extract the dark minerals (biotites and Fe-Ti oxides), the light minerals (quartz, sanidine, plagioclase), and the vesicles separately. The total amount of crystals

relative to the glass, and the proportion of dark (dense) minerals relative to white (less dense) minerals were estimated according to the surface they occupy.

(2) Density separation by panning. Samples were either ground with an agate mill, or crushed into particles less than 1 mm in diameter with a stainless steal hydraulic press. Water was poured on the samples in a panning dish, and glass was separated from the crystals due to its lower density. The volume fraction of crystals relative to glass was calculated according to the density difference between the glass and the crystals. Crystal density was estimated according to the relative proportion of light (average density considered ρ=2681 kg/m^3) and dark (average density considered ρ=3330 kg/m^3) minerals determined by image analysis. Glass density (2393 kg/m^3) was estimated using the temperature dependence of density defined by MELTS (Ghiorso and Sack 1995) between 800 and 900°C, extrapolated to room temperature. Dense rock equivalent (DRE) densities calculated using this glass density and these crystallinities are the same as those measured with the He-pycnometer (see next section), suggesting that the glass density, and therefore the crystallinities, obtained are correct.

Crystallinity estimation by panning should be the most reliable method (Cas and Wright 1988); however, as the density difference between non-vesiculated glass and the crystals is relatively small (<10%), crystal content can easily be slightly over- or underestimated. For frothy pumices with coarse vesicles, the crystallinity was overestimated (56 vol% crystals; Table 1) as bubble wall fragments, in the same order of size as the crystals, were not sufficiently light to be evacuated during panning. For the other pumice types, the crystallinity was rather underestimated as the smallest crystals were sometimes evacuated with the glass.

3.2 Porosity

Samples were drilled into cores about 2.5 cm in diameter and 1.5 to 3.5 cm high (74 cores in total). Each tube pumice sample was drilled parallel and perpendicular to vesicle elongation. Pumice cores were a bit irregular in shape due to the presence of large crystals of quartz that indented the sides of the core during drilling; therefore, the external volume of each pumice core was measured by fluid-displacement for more precision (Gardner et al. 1996). Samples were immersed in water with the help of a wire net on top of the beaker to avoid them from floating. The aim was to saturate the external pores (in about a day), to avoid water entering them during the fluid displacement measurement. During the procedure, samples are taken out of the saturation beaker, weighed, and immersed in another beaker to measure the volume. As some samples inhibit large pores, which are unlikely to keep the water during the weighing procedure, we systematically weighed the amount of water released on the scale and added this volume to the external volume of the core measured by water displacement. It appears that the volume of water released on the scale was very similar from a core to another, thereby suggesting that this process did not affect much the measurements.

Two types of vesicles can be distinguished: (1) connected and (2) isolated. We have measured *total porosity*, which is the total percentage of vesicles in a sample (i.e. connected vesicles + isolated vesicles), and *connected porosity*, which is the percentage of vesicles that are connected to each other and to the exterior (i.e. connected vesicles only). Total porosity was calculated using pumice densities and DRE densities. The DRE densities (ρ_{DRE}) were obtained by grinding some pumices of each type with an agate mill, weighing the powder, and measuring its volume with a Quantachrome He-stereopycnometer. The density of the pumice core (ρs_1) was calculated using the core's external volume (measured as explained above) and weight.

Connected porosity ($\Phi_{connected}$) was determined by measuring the volume of the core without the connected vesicles (equivalent to the volume of the glass and crystals with the isolated bubbles) with a Quantachrome He-stereopycnometer, and comparing it to the external volume of the core.

3.3 SEM imaging

To understand in greater detail the different porous media morphologies and the associated bubble dynamics, secondary electron scanning images of the different pumice types were observed. We used a Jeol JSM 6400 SEM at the University of Geneva at standard analytical conditions.

3.4 Hg-porosimetry

Hg-porosimetry is used to determine the pore-size distribution of porous material (including pumice; Witham and Sparks 1986), assuming pores are cylindrical. This method is based on the nonwetting characteristic of mercury: at a given pressure, surface tension will impede the entry of mercury into the pore spaces smaller than a certain diameter. The relationship between the pressure *P* and the radius *r* of the smallest filled pore is predicted by the Washburn equation:

$$r = \frac{2\gamma \cos\theta}{P} \qquad (1)$$

where γ and θ are the mercury surface tension and wetting angle respectively.

Measurements were done with a Thermo Electron Pascal 140 Hg-porosimeter on one frothy pumice (KPT04-26), one microvesicular pumice (KPT04-35) and three tube pumices (KPT04-5, 21, 27). During each analysis, a small fragment of the rock of interest (on the order of a few cm^3) was introduced into a sample holder filled with Hg at low pressure (~3 kPa/0.03 bar,

in our case). A gradually increasing external pressure (up to ~350 kPa, in our case) is then used to force mercury into the pores. The data obtained consists of the volume of Hg injected in the pores as a function of pressure. Pore size distributions are calculated with the Washburn equation, and these are plotted against the normalized volume of Hg (i.e. Cumulative volume of Hg injected in the pores at each step/Total volume of Hg injected in the pores over the entire analysis). We assume that bubble walls did not break at high pressure. This cannot be confirmed as a measurement on a rock fragment can only be performed once; Hg is not released entirely from the sample when the pressure is lowered at the end of the analysis.

3.5 Permeability measurements

The permeability of porous material is commonly measured using Darcy's law, which is only valid for low Reynolds number flow, wherein the relationship between the pressure gradient and the fluid velocity remains linear. This occurs when energy loss is entirely due to viscous effects. In our case, high flow rates were reached during analysis with an air permeameter (see next paragraph), implying additional energy loss to inertia due to non-laminar flow. The relationship between pressure gradient and fluid velocity thus becomes non-linear, and the Forchheimer equation must be used (Forchheimer 1901):

$$\frac{dp}{dz} = \frac{\mu}{k_1} v + \beta \rho v^2 \text{ with } \frac{dp}{dz} = \frac{\left(P_i^2 - P_0^2\right)}{2PL} \quad (2)$$

where P_i and P_0 are the fluid pressure at the entrance and exit of the medium respectively, P is the pressure of the fluid at which velocity and viscosity are measured or calculated (P_0 in this study), L is the sample length, μ and ρ are the fluid dynamic viscosity and density respectively, ν is the filter velocity (i.e. volumetric flow rate per total cross-sectional area of the sample orthogonal to fluid flow), k_1 is the viscous (or Darcian) permeability and β is a factor describing

inertial effects. As the factor β decreases, the resistance to flow from inertial effects decreases, and if $\beta \rightarrow 0$ the equation reduces to Darcy's law. The factor β corresponds to $1/k_2$ where k_2 is the inertial permeability used by Rust and Cashman (2004).

The permeability of KPT pumices was measured with a Porous Material Inc. gas (air) permeameter at the University of Geneva. The samples are the cores previously used for porosity measurements. They were inserted in a cylindrical chamber lined with rubber, and air was injected from the sides of the chamber to push the rubber against the sample and make it air-tight. The permeameter then injects air from the base of the chamber at an increasing pressure and flow rate. An apparent permeability was calculated using Darcy's law, and k_1 and β were calculated using the Forchheimer equation. A second degree polynomial curve was obtained by plotting the pressure gradient versus the filter velocity, and k_1 and β were derived from the coefficients (see also Rust and Cashman, 2004).

The permeameter was calibrated using a set of 10 standards. Capillary tubes of different diameters were embedded in epoxy plugs. The viscous permeability measured in the standards was compared to the predicted viscous permeability for laminar flow in tubes, which was calculated using equation (5) of Rust and Cashman (2004):

$$k_1 = \frac{\phi d^2}{32} \qquad (3)$$

where Φ is the porosity and d is the inner diameter of the cylindrical holes.

Measured β factors were compared to theoretical β factors, calculated as follows: Combining Forchheimer's law (2) and (3) yields:

$$\frac{dp}{dz} = \frac{32\mu}{d^2}u + \beta\rho\phi^2 u^2 \qquad (4)$$

where $u=v/\Phi$. Vertical pipe flow can be expressed as (Bird at al., 1960):

$$\frac{dp}{dz} = \rho g + 2\rho u^2 \frac{f}{d} \quad (5)$$

where u is the flow average velocity, g is the gravitational acceleration, and f is a friction factor given by:

$$f = \frac{16\mu}{d\,u\rho} + f_0 \quad (6)$$

where f_0 is an experimentally determined constant. With air as a gas, the first term of the right-hand side of (5) can be neglected. Combining (5) and (6) yields:

$$\frac{dp}{dz} = \frac{32\mu}{d^2} u + \frac{2\rho u^2}{d} f_0 \quad (7)$$

Thus, combining (4) and (7), we get:

$$\beta = \frac{2 f_0}{d\phi^2} \quad (8)$$

Using the data in Table 1 of Rust and Cashman (2004) we obtain f_0=0.025. There is good agreement between theoretical and measured k_1 and β values (Fig. 4).

4 Results

4.1 Crystallinity

Crystal contents range from 8% to 40% (Table 1). According to image analysis, tube and frothy pumices have similar amounts of crystals and they are the most crystal-rich. According to panning, frothy pumices are much more crystalline, but we assume that this is an artefact due to the method (as explained above). Grey-banded pumices and microvesicular pumices have low crystallinities compared to tube and frothy pumices.

4.2 Porosity

The four pumice types are distinguishable in a connected porosity versus total porosity plot (Fig. 5, Table 2), although some data overlap occurs between grey-banded and microvesicular pumices. Frothy pumices are more vesicular than tube pumices, but both types have well connected vesicles. Grey-banded pumices are generally poorly vesicular and exhibit the lowest vesicle connectivity of the four pumice types. Microvesicular pumices are very heterogeneous, and show a large spread in connected porosity; some samples only have a third of their vesicles connected, while others have all their vesicles connected. Microvesicular pumices were difficult to sample, as they are rare, fragile, and generally small. Ten cores coming from a ~40 cm-diameter microvesicular pumice yielded porosity values more spread out than all frothy or tube samples distributed across multiple stratigraphic levels, highlighting the heterogeneous nature of this type.

4.3 SEM imaging

SEM imaging of all four types of KPT pumices allows to clearly see incipient coalescence by bubble connection (Fig. 6). In tube pumices, bubble wall thinning can be seen between adjacent tubes, deforming slightly the generally circular diameter. Frothy pumices show some bubble connections although the general tendency is to deform into polyhedral cells. Grey-banded pumices have complex vesicle shapes with thin and stretched bubble wall remnants between coalesced vesicles. Small vesicles in microvesicular pumices are well connected with nearly spherical throats. In addition, microvesicular pumices display large cavities with microvesicles expanding into them (Fig. 6d). We assume a bimodal pore size distribution for this

pumice type, with microvesicles < 50 μm in diameter and cavities > 100 μm in diameter (marked "Cavity", Fig. 6e).

4.4 Hg-porosimetry

As most KPT pumices have bubble entrances (throats) that are smaller than the vesicles themselves, Hg-porosimetry will yield a distribution of pore access (throat) radii, rather than a pore size distribution. If the results are considered as a pore size distribution, the volume proportion of small vesicles will be overestimated: a large vesicle with a small entry diameter will be interpreted as a large number of small vesicles, with the same total volume. This is commonly referred to as the inkbottle effect (Abell et al. 1999; Salmas and Androutsopoulos 2001), and will be particularly acute for the frothy pumices.

We obtained pore access radii distributions from 250 μm to 2 μm, as pressure during our analyses ranged from 3 kPa to 350 kPa. According to this method, 90% of the pore access radii are smaller than 25 μm in the microvesicular pumices (Fig. 7). This suggests that the cavities observed in hand specimen have pore access radii in the same order of magnitude as the microvesicles (Fig. 6d), unless they are much larger (>250 μm) and cannot be discriminated by the Hg-porosimetry method. In contrast, frothy pumices have a larger fraction of pore access radii between 25 and 250 μm, although they do contain a significant proportion of pore access radii <25 μm. Tube pumices fall at intermediate positions; they contain fewer small pore access radii than the microvesicular pumices (~70% to 80% of their pore access radii are smaller than 25 μm). For tube pumices, pore access radii distribution is probably close to a true pore size distribution due to the almost cylindrical shape of the vesicles.

4.5 Permeability

Viscous permeability (k_1) in KPT pumice cores ranges from 10^{-14} to 10^{-11} m^2, and shows significant overlaps of data from the different pumice classes (Fig. 8a; Table 3). Despite the overlap in the permeability data, tendencies can be defined for each pumice class (Fig. 8c). Tube pumices measured parallel to vesicle elongation are the most permeable (average of $3*10^{-12}$ m^2), frothy pumices are slightly less so (average of $1*10^{-12}$ m^2), while grey-banded pumices and tube pumices measured perpendicular to vesicle elongation are the least permeable (average of $7*10^{-14}$ and $1*10^{-13}$ m^2 respectively), and microvesicular pumices show a large spread (from $1.5*10^{-14}$ to $6*10^{-12}$ m^2). Permeabilities of tube pumices measured parallel to vesicle elongation are systematically one to two orders of magnitude greater than those of tube pumices measured perpendicular to vesicle elongation (Fig. 8d), indicating that permeability does not depend exclusively on porosity, bubble connectivity, or throat size (Saar and Manga 1999). Permeability impedance due to tortuosity of flow paths (length of actual path/length of core) is needed to explain the difference (Wright et al. 2006).

The Forchheimer coefficient, β, theoretically contains information on the tortuosity of the flow paths, as tortuosity is the major mean of creating fluid-recirculation zones (i.e. turbulent flow; Ruth and Ma 1992). However, for this to be valid, the factor β must be an intrinsic property of the porous media and the flow must be turbulent (otherwise there are no inertial effects to be measured). After rewriting the Forchheimer equation, the apparent permeability (i.e. permeability calculated using Darcy's law) is defined as (Huang and Ayoub 2006):

$$\frac{1}{k_a} = -\frac{\partial p}{\partial x}\frac{1}{\mu v} = \frac{1}{k_1} + \beta\frac{\rho v}{\mu} \qquad (9)$$

The relationship between 1/Ka and $\rho v/\mu$ is controlled by the variability of the factor β over the filter velocity range. The variability of the factor β was examined for the standards, and for seven samples (Fig. 9a). Linear relationships with positive slopes were obtained for the nine standards with the greatest capillary tube diameters, and for the frothy and tube pumices measured parallel to vesicle elongation, suggesting that β was constant in the range of interest. The standard with the smallest capillary tube diameter (0.20 mm; i.e. least permeable), and the microvesicular, grey-banded and tube pumices measured perpendicular to vesicle elongation define concave up curves. This behaviour could be due to the absence of turbulence during flow; therefore, the relationships between the inverse apparent permeability and the Reynolds number ($Re = \rho v d/\mu\phi$) were examined for the standards (Fig. 9b). When Re is < 2000, the flow is laminar, and the factor β should vanish. The Re number is only smaller than 2000 in the standard with the smallest capillary tube diameter (0.20 mm), confirming that flow was laminar during this analysis. As the microvesicular, grey, and tube pumices measured perpendicular to vesicle elongation display a similar trend in Figure 9a, we believe that flow was laminar in these samples as well. The factor β is thus significant only for the frothy pumices and the tube pumices measured parallel to vesicle elongation. The factor β is larger in frothy pumices than in tube pumices measured parallel to vesicle elongation (Fig. 10). This suggests greater inertial effects hence greater tortuosity in frothy pumices.

5 Discussion

The connected porosity-permeability relationship proposed by Klug and Cashman (1996) does not fit our entire data set. Tube pumices measured parallel to vesicle elongation plot well above the upper limit that bounds most of the Klug and Cashman (1996) data, and

389 microvesicular pumices are so heterogeneous that no relationship between connected porosity
390 and permeability can be determined.

391 Mueller et al. (2005) defined two types of relationships between permeability and total
392 porosity (Fig. 8b). The first one uses a Kozeny-Carman relationship to describe flow in tube-
393 shaped porous media corresponding to effusive material, and the second one applies a theoretical
394 fully penetrable spheres percolation model (FPS) to describe flow in a porous media
395 characterized by spheres. Frothy pumices are well described by the FPS model, as would be
396 expected from the large spherical vesicles that form the porous media. Data for tube pumices
397 measured parallel to vesicle elongation are bounded by the two sets of curves confirming their
398 hybrid pore structures that mimic tubes (similar to the Campi Flegrei and Pinatubo pumices
399 described in Mueller et al., 2005). Grey-banded pumices and tube pumices measured
400 perpendicular to vesicle elongation are less permeable than predicted by either model, although
401 slightly better represented by the FPS, and microvesicular pumices show no correlation between
402 total porosity and permeability. This suggests that their porous media cannot be simply
403 represented by tubes or spheres.

404 In this section, we shall mainly focus on the pumices originated from the crystal-rich
405 magma (i.e. tube and frothy pumices), as they are by far the most abundant (> 99 vol% of the
406 total amount of pumiceous material produced by the KPT).

407 *5.1 Tube and frothy pumices*

408 Tube and frothy pumices have the same geochemical composition, mineralogy and a
409 similar range in crystallinity (~25-30 vol% crystals, if we assume that the panning method for the
410 frothy pumice overestimates the crystal content), implying that they originated from the same

411 magma batch. The presence of both types of pumices, with a gradation from pumices with tube-
412 shaped vesicles to pumices with spherical vesicles in Units D and E reinforces this inference.
413 Hence, we attribute the significant differences in total porosity, connected porosity, permeability
414 and β factor between them to differences in the amount of shearing each pumice type
415 experienced while ascending in the volcanic conduit. Below, we review the impacts shearing had
416 on the petrophysical properties of these two pumice types:

417 (1) Shearing enhanced coalescence (Stasiuk et al. 1996; Okumura et al. 2006): vesicles in
418 frothy pumices had to reach the maximum packing of spheres (~74-83% vesicles; Klug
419 and Cashman, 1996) to reach the same bubble connectivity as the tube pumices, and even
420 then, vesicles had the tendency to deform into polyhedral cells rather than coalescing
421 (Fig. 6).

422 (2) Shearing reduced the amount of inertial effects that developed during gas flow through
423 the magmatic foam: The data show that (1) the factor β is larger in frothy pumices than in
424 tube pumices, and (2) with the same degree of bubble connectivity and lower connected
425 porosities, tube pumices still have larger viscous permeabilities than do frothy pumices.
426 Due to shearing, flow paths in tube pumices are numerous, and tortuosity is low, as
427 vesicles have been stretched and aligned (Fig. 11d). Moreover, pore throats in tube
428 pumices resemble more venturi models than orifice models used in fluid mechanics (Ruth
429 and Ma 1992; Fig. 11a), thereby lowering inertial effects. On the opposite, flow paths in
430 frothy pumices are less connected and more tortuous (Fig. 11c). Pore throats are closer to
431 orifice models (Fig. 11b), thereby increasing inertial effects.

(3) As it increases coalescence and decreases tortuosity, shearing favours the early development of a permeable network. Therefore, more intensely sheared pumices display a higher permeability despite a significantly lower total porosity than the frothy pumices.

To understand how magma grows bubbles and degasses during ascent, we need to understand how shearing is distributed throughout the volcanic conduit. A tube-shaped vesicle can be generated either by (a) simple or (b) pure shear of a spherical vesicle (e.g., Rust et al., 2003). Both types of shear can occur during volcanic eruptions. Simple shear is obtained with a horizontal velocity gradient across the conduit (e.g., Poiseuille flow), whereas pure shear is obtained due to the acceleration of magma in the conduit. In light of this, we propose two eruption models that could have generated both the tube and the frothy pumice types, and discuss them according to field observations (Figure 12).

(1) Simple Shear: Velocity profiles across a conduit are found to be parabolic or plug-flow (e.g., Llewellin et al. 2002; Polacci et al. 2003; Mastin 2005; Gonnermann and Manga, 2007). In both cases, simple shearing occurs due to higher velocities in the centre than at the margins of the conduit. In the case of a plug-shaped velocity profile, simple shearing is more intense on the margins than in the centre, leading to a *horizontally* zoned conduit in terms of vesicle morphology (Llewellin et al. 2002; Fig. 12a).

If strain rates were dominated by simple shear in the conduit, synchronously producing both tube and frothy pumices is straightforward. Tube pumices would be formed at the edges of the conduit, where shear was highest, and frothy pumices would form in the low-shear plug-flow zone in the centre. This model is supported by the observation of a section across a conduit at the Mule Creek vent (Stasiuk et al. 1996), where sub-rounded vesicles are found in the centre and flattened/lensoidal vesicles at the margins.

455 The relative amount of frothy pumices and tube pumices will be determined by the size of
456 the low shear region relative to the size of the conduit, which depends on the conduit Capillary
457 number Cc (e.g., Llewellin et al., 2002)

458 $$Cc = \frac{P' R \lambda}{\mu} \quad (10)$$

459 where P' is the pressure gradient, R the radius of the conduit, λ the bubble relaxation time, and μ
460 the magma viscosity. Assuming that the pressure gradient, the bubble relaxation time, and the
461 magma viscosity remain roughly similar at fragmentation, an increase in conduit radius would
462 shift the conduit Capillary number from low to intermediate-high values, which would promote
463 the co-existence of both frothy and tube pumices by enlarging the low-shear plug-flow region in
464 the centre of the conduit. This scenario would be consistent with the observed appearance of
465 frothy pumice only in the climactic, highest eruption rate period of the eruption (unit D and E)
466 (Dufek and Bergantz 2007). The influence of a possible shift from an early sub-circular vent to
467 fissural, ring-fractures during the caldera-forming stage (e.g, Wilson and Hildreth 1997) is
468 expected to decrease the frothy/tube ratio (fissures have higher internal conduit surface over the
469 conduit volume) but wide-enough fissures would still potentially be able to sustain a low-strain
470 central region in the conduit.

471 Considering a conduit dominated by simple shear, gas escape from the permeable magma
472 foam is expected to occur at the conduit margins relative to the centre, and parallel to magma
473 flow (as previously suggested by Blower 2001; Gonnermann and Manga 2003; Rust et al. 2003;
474 Wright et al. 2006). Horizontal gas escape into wall rocks should be minor as permeability in
475 tube pumices is 1-2 orders of magnitude smaller in the direction perpendicular to vesicle
476 elongation.

(2) Pure shear: Along the conduit, pressure decreases, leading to gas exsolution and bubble growth. As a result, magma will be forced to accelerate and elongational strain rate will increase (Papale 1999). During magma ascent, vesicles will remain spherical until the elongational strain is sufficient to stretch them. The conduit then becomes *vertically* zoned in terms of vesicle morphology, with tube pumices overlying frothy pumices (Fig. 12b).

If strain rates were dominated by pure shear in the conduit, synchronously producing tube and frothy pumices requires that the fragmentation occur over a significant thickness of magma so as to fragment both the elongated vesicle- and the deeper-seated spherical vesicle-bearing regions (Figure 12b). The relative abundance of frothy pumices is determined by the thickness of the fragmentation zone. To explain the observed pumice type distribution in the KPT by this mechanism, the fragmentation thickness must have been small at the beginning of the eruption (Units A to C, no frothy pumices), large during the maximum mass discharge rate (Units D and E), and small again during the waning phase of the eruption (Unit F, no frothy pumices). During the "thick fragmentation" phase, we expect the eruption to have high-frequency pulses, as, once the magma batch containing both types of vesicles has been fragmented, some time is required to stretch the following ascending vesicles.

On the basis of the current understanding, we cannot convincingly rule out a particular style of shear in the conduit. Both probably play a role, and the observations made on the KPT pumices do not favour either set-up. Determining more precisely the style and the thickness of the fragmentation zone and the shape of the velocity profile close to fragmentation is a research avenue that will further refine our understanding of magma flow in volcanic conduits.

5.2 Microvesicular pumices

Despite having the same chemical composition and the same mineralogy (but different crystal content), microvesicular pumices are petrophysically distinct from tube and frothy pumices by virtue of their bimodal pore size distributions (they are dominantly microvesicular but also contain some mm-size cavities), very variable porosity (due to the presence/absence of cavities in the core analysed), and permeability. They were synchronously erupted with tube pumices, implying that different eruption rates, variable interactions with seawater, and/or fragmentation depth cannot be the main factors responsible for these differences. The presence of large cavities could have been produced by bubble coalescence. However, such a scenario appears unlikely for a rhyolitic plinian eruption as magma is generally quenched before bubble wall retraction and re-rounding occurs (Gonnermann and Manga 2007).

The bimodal vesicle size distribution is traditionally attributed to two stages of bubble nucleation and growth (Sparks and Brazier 1982, Whitam and Sparks 1986). In agreement with the observation of a bimodal vesicle population, we suggest that small bubbles in microvesicular pumices were produced by a late event of homogeneous nucleation. The fact that homogeneous bubble nucleation can be observed in laboratory experiments in the presence of a first heterogeneous bubble nucleation event along the walls of the experimental charge, suggests that both types of bubble nucleation can also occur in a same batch of magma (Mangan et al., 2004). Mangan et al. (2004) suggest that early heterogeneous bubble nucleation may occur at depth using Fe-Ti oxides and biotites as nucleation sites, and homogeneous bubble nucleation follows in response to high super-saturation as the magma ascends. In the microvesicular pumices, the early heterogeneous bubble nucleation event would have generated the large cavities, whereas the later homogeneous bubble nucleation event would have generated the small diameter bubble

population (microvesicles). Inthis scenario, the later nucleation would have been enabled by the low crystallinity of the magma (Massol and Koyaguchi 2005), which explains the absence of small, isolated vesicles in the tube and frothy pumices.

6 Summary

The study of the pumice types generated by the KPT eruption shows that large rhyolitic eruptions can produce different types of pumices, which acquire their distinct petrophysical characteristics (connected porosity, permeability and β factor) mostly during the ascent in the conduit (see also Marti et al, 1999; Polacci et al., 2001). The KPT pumice types (similar to those defined by Allen, 2001) include, in order of abundance, (1) crystal-rich tube pumices (by far the most common type), (2) crystal-rich frothy pumices, (3), microvesicular pumices with a bimodal bubble size distribution and (4) grey-banded pumices. Crystallinity, porosity and permeability measurements, which consider the development of inertial effects during analysis, allow us to interpret the differences between pumice types in terms of processes by which permeable networks develop in conduits during eruption. We infer that the distinction between the two types of crystal-rich pumices is due to shearing (either simple or pure shear), that (1) favoured coalescence, (2) straitened flow paths and thereby reduced the development of inertial effects during gas flow through the magmatic foam, and thus (3) allowed the earlier development of a permeable network in tube pumices relative to frothy pumices. On the other hand, the differences between the crystal-poor and the crystal-rich pumices are inferred to the occurrence of a homogeneous bubble nucleation event in the former and not in the latter.

ACKNOWLEDGMENTS

This project was supported by the Swiss NSF grant #2000-103441/1 to Bachmann. CBdM thanks the Bourse Lombard for contributing to field expenses. The Greek Institute of Geology & Mineral Exploration graciously provided a permit to work in the area. We thank Georges E. Vougioukalakis for his logistical guidance, E. Davaud for providing access to his petrophysical laboratory, G. Overney for his help with the permeameter, and J.M. Boccard for making the permeability standards.

7 References

Abell AB, Willis KL, Lange DA (1999) Mercury Intrusion Porosimetry and Image Analysis of Cement-Based Materials. J. Colloid Interface Sci. 211:39-44

Allen SR (1998) Volcanology of the Kos Plateau Tuff, Greece: the product of an explosive eruption in an archipelago, Ph.D. Thesis, Monash University, Australia.

Allen SR (2001) Reconstruction of a major caldera-forming eruption from pyroclastic deposit characteristics: Kos Plateau Tuff, eastern Aegean Sea. J. Volcanol. Geotherm. Res. 105:141-162

Allen SR, Cas RAF (1998a) Lateral variations within coarse co-ignimbrite lithic breccias of the Kos Plateau Tuff, Greece. Bull. Volcanol. 59:356-377

Allen SR, Cas RAF (1998b) Rhyolitic fallout and pyroclastic density current deposits from a phreatoplinian eruption in the eastern Aegean sea, Greece. J. Volcanol. Geotherm. Res. 86:219-251

Allen SR, Stadlbauer E, Keller J (1999) Stratigraphy of the Kos Plateau Tuff: product of a major Quaternary explosive rhyolitic eruption in the eastern Aegean, Greece. Int Journ Earth Sciences 88:132-156

563 Bird RB, Stewart WE, Lightfoot EN (1960) Transport Phenomena. John Wiley, New York,
564 780pp
565 Blower JD (2001) Factors controlling permeability-porosity relationships in magma. Bull.
566 Volcanol. 63:497-504
567 Cas RAF, Wright JV (1988) Modern and ancient volcanic successions. Chapman &Hall,
568 London, pp 1-528
569 Geotherm. Res. 143(1-3):113-132
570 Dufek J, Bergantz GW (2007) Dynamics and deposits of the Kos Plateau Tuff eruption: Controls
571 of basal particle loss on pyroclastic flow transport. Geochem. Geophy. Geosystems 8:Q122007
572 Eichelberger JC, Carrigan CR, Westrich HR, Price RH (1986) Non-explosive silicic volcanism.
573 Nature 323(October):598-602
574 Forchheimer P (1901) Wasserbewegung durch Boden. Z. Ver. Dtsch. Ing. 45:1781-1788
575 Gardner JE, Thomas RME, Jaupart C, Tait S (1996) Fragmentation of magma during Plinian
576 volcanic eruptions. Bull. Volcanol. 58:144-146
577 Ghiorso MS, Sack RO (1995) Chemical Mass Transfer in Magmatic Processes. IV. A Revised
578 and Internally Consistent Thermodynamic Model for the Interpolation and Extrapolation of
579 Liquid-Solid Equilibria in Magmatic Systems at Elevated Temperatures and Pressures. Contrib.
580 Mineral. Petrol. 119:197-212
581 Gonnermann HM, Manga M (2003) Explosive volcanism may not be an inevitable consequence
582 of magma fragmentation. Nature 426:432-435
583 Gonnermann HM, Manga M (2007) The fluid mechanics inside a volcano. Annu. Rev. Fluid
584 Mech. 39:321-356

585 Huang H, Ayoub J (2006) Applicability of the Forchheimer equation for non-Darcy flow in
586 porous media. Society of Petroleum Engineers SPE 102715
587 Jaupart C (1998) Gas loss from magmas through conduit walls during eruption. Spec. Publ. Geol.
588 Soc. London 145:73-90
589 Jaupart C, Allègre CJ (1991) Gas content, eruption rate and instabilities of eruption regime in
590 silicic volcanoes. Earth Planet. Sci. Lett. 102:413-429
591 Jouniaux L, Bernard ML, Zamora M, Pozzi JP (2000) Streaming potential in volcanic rocks from
592 Mount Pelée. J. Geophy. Research 105(B4):8391-8401
593 Klug C, Cashman KV (1996) Permeability development in vesiculating magmas: implications
594 for fragmentation. Bull. Volcanol. 58:87-100
595 Klug C, Cashman KV, Bacon CR (2002) Structure and physical characteristics of pumice from
596 the climactic eruption of Mount Mazama (Crater Lake), Oregon. Bull. Volcanol. 64:486-501
597 Llewellin EW, Mader HM, Wilson SDR (2002) The constitutive equation and flow dynamics of
598 bubbly magmas. Geophy. Res. Letters 29:24,2170
599 Mangan M, Mastin L, Sisson T (2004) Gas evolution in eruption conduits: combining insights
600 from high temperature and pressure decompression experiments with steady-state flow
601 modelling. J. Volcanol. Geotherm. Res. 129:23-36
602 Marti J, Soriano C, Dingwell DB (1999) Tube pumices as strain markers of the ductile-brittle
603 transition during magma fragmentation. Nature 402(6762):650-653
604 Massol H, Koyaguchi T (2005) The effect of magma flow on nucleation of gas bubbles in a
605 volcanic conduit. J. Volcanol. Geotherm. Res. 143:69-88
606 Mastin L (2005) The controlling effect of viscous dissipation on magma flow in silicic conduits.
607 J. Volcanol. Geotherm. Res. 143:17-28

608 Melnik O (2000) Dynamics of two-phase conduit flow of high-viscosity gas-saturated magma:
609 large variations of sustained explosive eruption intensity. Bull. Volcanol. 62(3):153-170
610 Melnik O, Barmin A, Sparks RSJ (2005) Dynamics of magma flow inside volcanic conduits with
611 bubble overpressure buildup and gas loss through permeable magma. J. Volcanol. Geotherm.
612 Res. 143(1-3):53-68
613 Melnik O, Sparks RSJ (2002) Dynamics of magma ascent and lava extrusion at Soufrière Hills
614 Volcano, Montserrat. Geol. Soc. London, Memoirs 21:153-171
615 Mueller S, Melnik O, Spieler O, Scheu B, Dingwell DB (2005) Permeability and degassing of
616 dome lavas undergoing rapid decompression: An experimental determination. Bull. Volcanol.
617 67:526-538
618 Okumura S, Nakamura M, Tsuchiyama A (2006) Shear-induced bubble coalescence in rhyolitic
619 melts with low vesicularity. Geophy. Res. Letters 33:L20316
620 Papale P (1999) Strain-induced magma fragmentation in explosive eruptions. Nature 397:425-
621 428
622 Papale P (2001) Dynamics of magma flow in volcanic conduits with variable fragmentation
623 efficiency and nonequilibrium pumice degassing. J. Volcanol. Geotherm. Res. 106(B6):11043-
624 11065
625 Polacci M, Papale P, Rosi M (2001) Textural heterogeneities in pumices from the climactic
626 eruption of Mount Pinatubo, 15 june 1991, and implications for magma ascent dynamics. Bull.
627 Volcanol. 63:83-97
628 Polacci M, Pioli L, Rosi M (2003) The Plinian phase of the Campanian Ignimbrite eruption
629 (Phlegrean Fields, Italy): evidence from density measurements and textural characterization of
630 pumice. Bull. Volcanol. 65:418-432

631 Roduit N (2006) JMicroVision: Image analysis toolbox for measuring and quantifying
632 components of high-definition images. http://www.jmicrovision.com Version 1.2.2. (accessed 2
633 July 2006)
634 Rust AC, Cashman KV (2004) Permeability of vesicular silicic magma: inertial and hysteresis
635 effects. Earth Planet. Sci. Lett. 228:93-107
636 Rust AC, Manga M, Cashman KV (2003) Determining flow type, shear rate and shear stress in
637 magmas from bubble shapes and orientations. J. Volcanol. Geotherm. Res. 122:111-132
638 Ruth D, Ma H (1992) On the derivation of the Forchheimer equation by means of the averaging
639 theorem. Transport in Porous Media 7:255-264
640 Saar MO, Manga M (1999) Permeability-porosity relationship in vesicular basalts. Geophy. Res.
641 Letters 26(1):111-114
642 Salmas C, Androutsopoulos G (2001) Mercury Porosimetry: Contact Angle Hysteresis of
643 Materials with Controlled Pore Structure. J. Colloid Interface Sci. 239:178-189
644 Slezin YB (2003) The mechanism of volcanic eruptions (a steady state approach). J. Volcanol.
645 Geotherm. Res. 122(1-2):7-50
646 Smith PE, York D, Chen Y, Evensen NM (1996) Single crystal ^{40}Ar-^{39}Ar dating of a Late
647 Quaternary paroxysm on Kos, Greece: Concordance of terrestrial and marine ages. Geophy. Res.
648 Letters 23(21):3047-3050
649 Sparks RSJ, Brazier S (1982) New evidence for degassing process during explosive eruptions.
650 Nature 295:218-220
651 Stadlbauer E (1988) Vulkanologisch-geochemische analyse eines jungen ignimbrites: Der Kos-
652 Plateau-Tuff (Südost-Ägäis). Ph.D. Thesis, Freiburg, 182pp.

653 Stasiuk MV, Barclay J, Carroll MR, Jaupart C, Ratté JC, Sparks RSJ, Tait SR (1996) Degassing
654 during magma ascent in the Mule Creek vent (USA). Bull. Volcanol. 58:117-130
655 Thomas N, Jaupart C, Vergniolle S (1994) On the vesicularity of pumice. J. Geophy. Research
656 99(B8):15633-15644
657 Wilson CJN, Hildreth W (1997) The Bishop Tuff: New insights from eruptive stratigraphy. J.
658 Geology 105:407-439
659 Witham AG, Sparks RSJ (1986) Pumice. Bull. Volcanol. 48:209–223
660 Woods AW, Koyaguchi T (1994) Transitions between explosive and effusive volcanic eruptions.
661 Nature 370:641-644
662 Wright HMN, Roberts JJ, Cashman KV (2006) Permeability of anisotropic tube pumice: Model
663 calculations and measurements. Geophy. Res. Letters 33(L17316):1-6

8 Illustrations and Tables

8.1 Figure captions

Figure 1: Map of the Aegean region, showing the main volcanic centres of the modern Aegean Arc, and a GoogleEarth close-up on the Kos-Nisyros area, with approximate locations (stars) and types of samples used in this study The dashed rectangle on the regional map in the lower left corner corresponds to the extension of the GoogleEarth picture.

Figure 2: Variation in eruption intensity with time during the KPT eruption, and distribution of the different pumice types within the KPT deposits (modified from Fig. 11 in Allen, 2001).

Figure 3: Selected thin sections of the four pumice types in the KPT. (a) Crystal-rich tube pumice, parallel to vesicle elongation. Vesicle stretching direction is emphasized by the red double-head arrow. (b) Crystal-rich tube pumice, perpendicular to vesicle elongation. (c) Crystal-rich frothy pumice. (d) Crystal-poor, microvesicular pumice, showing mostly small vesicles, but also displaying mm-sized cavities (marked “cavity”). (e) Grey-banded pumice. Note the colour banding implying a mix between two different magmas.

Figure 4: Theoretical vs. measured viscous permeability (a) and β factor (b). There is good agreement between theoretical and measured values.

Figure 5: Connected porosity vs. total porosity for the different types of KPT pumices. Error is smaller than symbol size. Straight line represents total connection of the vesicles and dashed lines represent contours of the volume percentage of connected vesicles in the pumice. Tube and frothy pumices are the most connected. Microvesicular pumices are very heterogeneous.

686 *Figure 6*: SEM images of the four different pumice types. All scale bars correspond to
687 100 μm. (a) Tube pumice sample cut perpendicular to vesicle elongation. Note the sub-circular
688 vesicle sections, except where bubble walls are thinning just prior to coalescence of adjacent
689 bubbles (in the white circle). (b) Frothy pumice. Note the size of the vesicles and the
690 development of polyhedral cells. The first steps of bubble coalescence can be seen where bubble
691 walls are ruptured (arrows) (c) Detailed view of a large vesicle developed by coalescence in a
692 grey-banded pumice. Note the presence of thin filaments due to incomplete bubble wall
693 retraction. (d) Detailed view of the vesicle network in a microvesicular pumice. Note the high
694 degree of bubble connectivity and the remarkably circular throats. (e) Less detailed view of the
695 same microvesicular pumice, arrows show small vesicles coalescing into larger cavity-type
696 vesicles.

697 *Figure 7*: Pore access radii distributions obtained by Hg-porosimetry for a microvesicular
698 pumice, a frothy pumice and the three tube pumices. Microvesicular pumices have the largest
699 amount of more small (<25 μ) pore access radii, while frothy pumices show much larger pore
700 access radii.

701 *Figure 8*: (a) Viscous permeability vs. connected porosity; bold, dash-point line
702 represents the relationship suggested by Klug and Cashman (1996) (perm = $2x10^{-19}$ $ves^{3.5}$), and
703 light coloured dash-point lines represent upper and lower limits bounding most of their data. (b)
704 Viscous permeability vs. total porosity; curves were defined by Mueller et al. (2005), based on
705 Kozeny-Carman relationships representative of flow in tubes (dashed lines), and a fully
706 penetrable spheres percolation model (FPS) representative of flow in a porous media
707 characterized by spheres (bold and light coloured lines). (c) Average viscous permeability vs.
708 average connected porosity for pumice types and (d) permeability comparison between tube

pumices measured parallel and perpendicular to vesicle elongation. Notice that tube pumices measured parallel to vesicle elongation are systematically more permeable than tube pumices measured perpendicular to vesicle elongation. In all graphs, error is smaller than symbol size.

Figure 9: (a) Inverse apparent permeability vs. filter velocity for the six smallest standards and seven samples; Straight lines with positive slopes are obtained for the 9 largest standards as well as for frothy (red) and tube pumices (blue) measured parallel to vesicle elongation, implying that the factor β is constant during analysis for these samples. (b) Inverse apparent permeability vs. Reynolds number for the ten standards; maximum error on Re is ~5% for Re = 2000 and ~20% for Re = 10000. Re numbers smaller than 2000 are only obtained for the smallest standard (0.20 mm) suggesting it is the only standard in which laminar flow occurred.

Figure 10: Forchheimer β factor versus connected porosity for frothy and tube pumices measured parallel to vesicle elongation. Error is smaller than symbol size. Greater values are observed for frothy pumices than for tube pumices measured parallel to vesicle elongation implying more inertial effects occur in the former than in the latter.

Figure 11: (a) Orifice model and (b) venturi model of pipes used in fluid mechanics. Inertial effects will be greater in the orifice model than in the venturi model, during flow. Scanned thin sections of (c) a frothy pumice with pore throats resembling the orifice model and (d) a tube pumice with pore throats resembling the venturi model, suggest that the inertial effects will be larger in the former than in the latter. The red arrows indicate possible flow paths.

Figure 12: Conduit sections illustrating the generation of tube pumices by simple shear (a) or pure shear (b) of the magma during eruption. In (a) simple shearing occurs due to higher velocities in the centre than at the margins of the conduit. In the case of a plug-shaped velocity

profile (as drawn here), simple shearing is more intense on the margins than in the centre, leading to a *horizontally* zoned conduit in terms of vesicle morphology (Llewellin et al. 2002, Polacci et al. 2003). Tube pumices are generated at the margins and frothy pumices in the centre of the conduit. In (b) pure shearing occurs due to the acceleration of the magma driven by bubble expansion following decompression. During magma ascent, vesicles will remain spherical until the elongational strain is sufficient to stretch them, leading to a *vertically* zoned conduit in terms of vesicle morphology, with tube pumices overlying frothy pumices.

8.2 Table captions

Table 1: Crystallinities of the four different types of KPT pumices. Crystal percentage is always on a bubble free basis. Abbreviations: Cryst. = crystallinities and Nb TS = number of thin sections.

Table 2: Main porosity characteristics of the four types of pumices preserved in the KPT. Abbreviations: Φ_T = total porosity, Φ_C = connected porosity, CV = proportion of vesicles that are connected, IV = volume percentage of isolated vesicles.

Table 3: Characteristics of the permeability standards: inner diameter of capillaries, porosity, measured and theoretical k1 and β.

8.3 Tables

Table 1

Pumice type	JMicroVision		Panning	
	Nb TS	Cryst.	Panned weight	Cryst.
Tube	2	24%	300g	30%
Frothy	4	24%	200g	56%
Microvesicular	3	11%	170g	5%
Grey-banded	1	13%	115g	13%

Table 2

		Grey-banded	Microvesicular	Frothy	Tube
	Average	**62**	**73**	**81**	**64**
Φ_T (%)	Minimum	51	63	78	59
	Maximum	70	79	84	72
	Average	**37**	**50**	**74**	**58**
Φ_C (%)	Minimum	24	14	63	49
	Maximum	47	78	81	68
	Average	**59**	**67**	**92**	**90**
CV (%)	Minimum	40	23	79	81
	Maximum	78	98	99	98
	Average	**25**	**23**	**7**	**7**
IV (%)	Minimum	12	1	1	1
	Maximum	39	49	17	11

Table 3

	d (mm)	Φ (%)	measured values		theoretical values	
			k_1 (m^2)	β (m^{-1})	k_1 (m^2)	β (m^{-1})
Std_188	1.88	0.566	$6.3*10^{-10}$	$6.6*10^{5}$	$6.25*10^{-10}$	$8.3*10^{5}$
Std_116	1.16	0.215	$2.1*10^{-11}$	$9.9*10^{6}$	$9.05*10^{-11}$	$9.3*10^{6}$
Std_100	1.00	0.160	$1.8*10^{-11}$	$2.2*10^{7}$	$5.00*10^{-11}$	$2.0*10^{7}$
Std_080	0.80	0.102	$2.4*10^{-11}$	$4.7*10^{7}$	$2.05*10^{-11}$	$6.0*10^{7}$
Std_068	0.68	0.074	$1.1*10^{-11}$	$1.2*10^{8}$	$1.07*10^{-11}$	$1.3*10^{8}$
Std_060	0.60	0.058	$2.2*10^{-11}$	$3.3*10^{8}$	$6.48*10^{-12}$	$2.5*10^{8}$
Std_051	0.51	0.042	$3.2*10^{-12}$	$6.0*10^{8}$	$3.38*10^{-12}$	$5.7*10^{8}$
Std_048	0.48	0.037	$4.8*10^{-12}$	$1.4*10^{9}$	$2.65*10^{-12}$	$7.7*10^{8}$
Std_043	0.43	0.030	$7.2*10^{-12}$	$1.3*10^{9}$	$1.71*10^{-12}$	$1.3*10^{9}$
Std_020	0.20	0.006	$5.2*10^{-14}$	$3.7*10^{10}$	$8.00*10^{-14}$	$6.1*10^{10}$

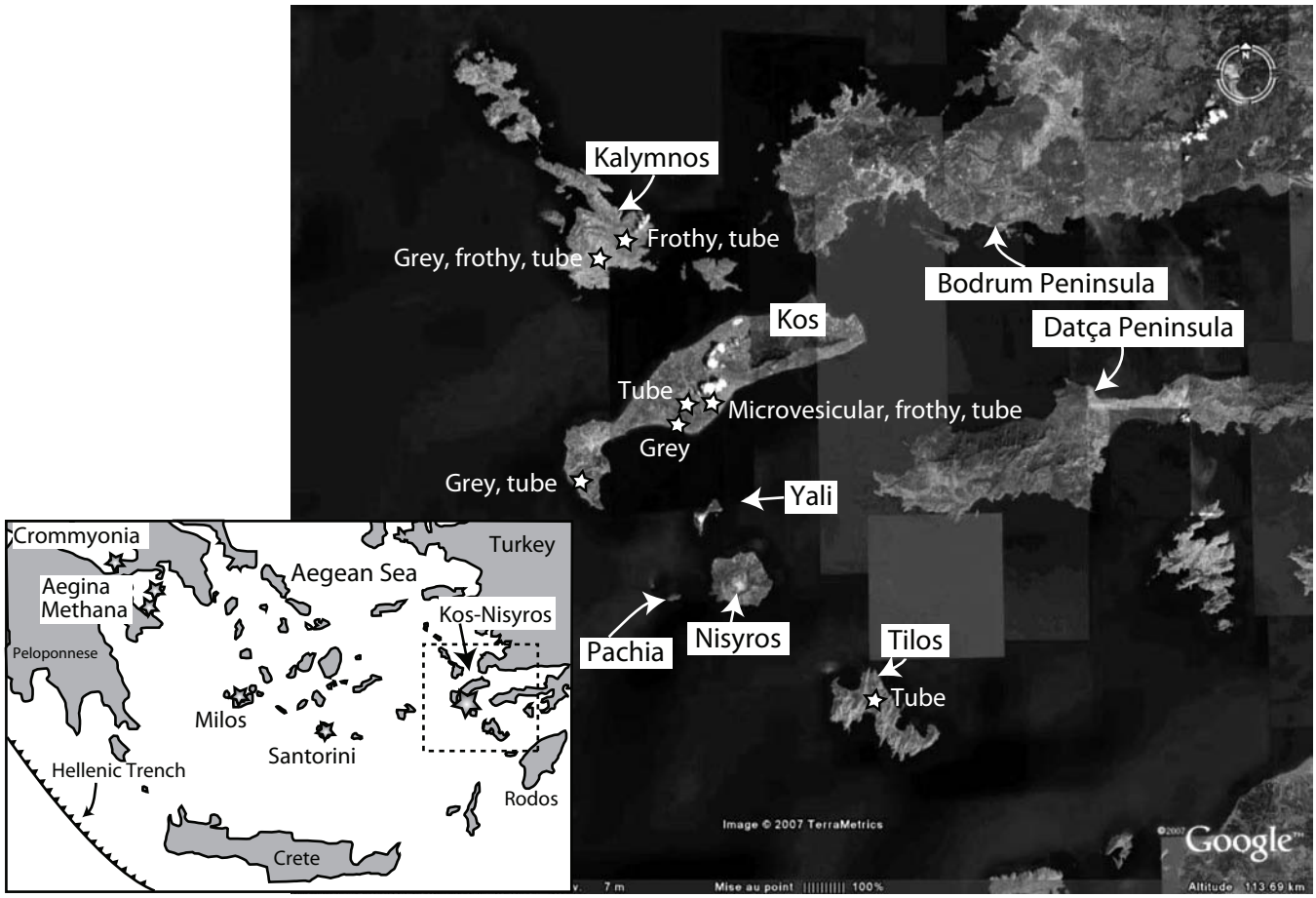
Kalymnos
Frothy, tube
Grey, frothy, tube
Bodrum Peninsula
Kos
Datça Peninsula
Tube
Microvesicular, frothy, tube
Grey
Grey, tube
Yali
Pachia
Nisyros
Tilos
Tube
Crommyonia
Turkey
Aegean Sea
Aegina
Methana
Kos-Nisyros
Peloponnese
Milos
Santorini
Hellenic Trench
Rodos
Crete
Image © 2007 TerraMetrics
Google
Mise au point
100%
Altitude 113 69 km

Figure 1

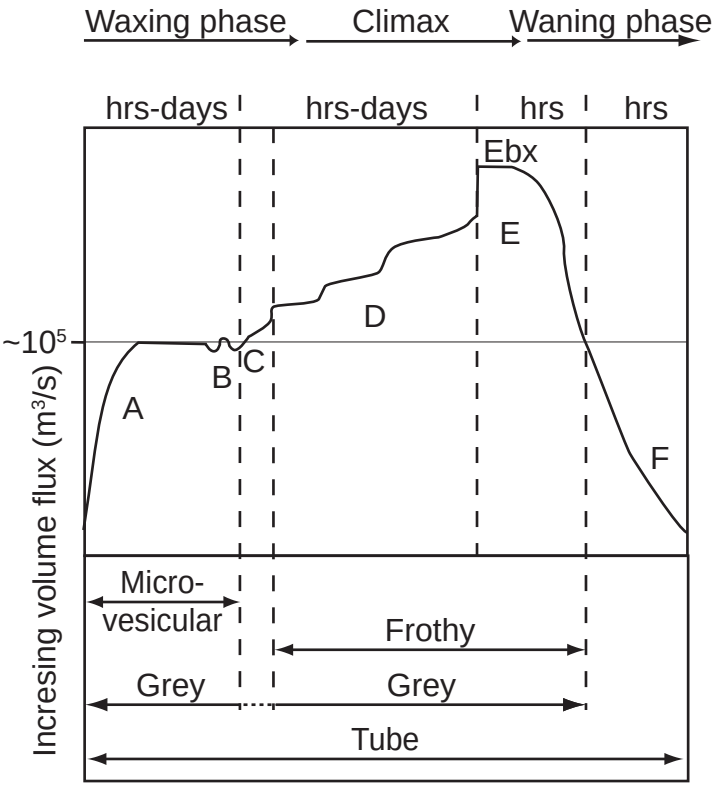
Waxing phase
Climax
Waning phase
hrs-days
hrs-days
hrs
hrs
Ebx
E
D
~10⁵
C
B
A
F
Incresing volume flux (m³/s)
Micro-
vesicular
Frothy
Grey
Grey
Tube

Figure 2

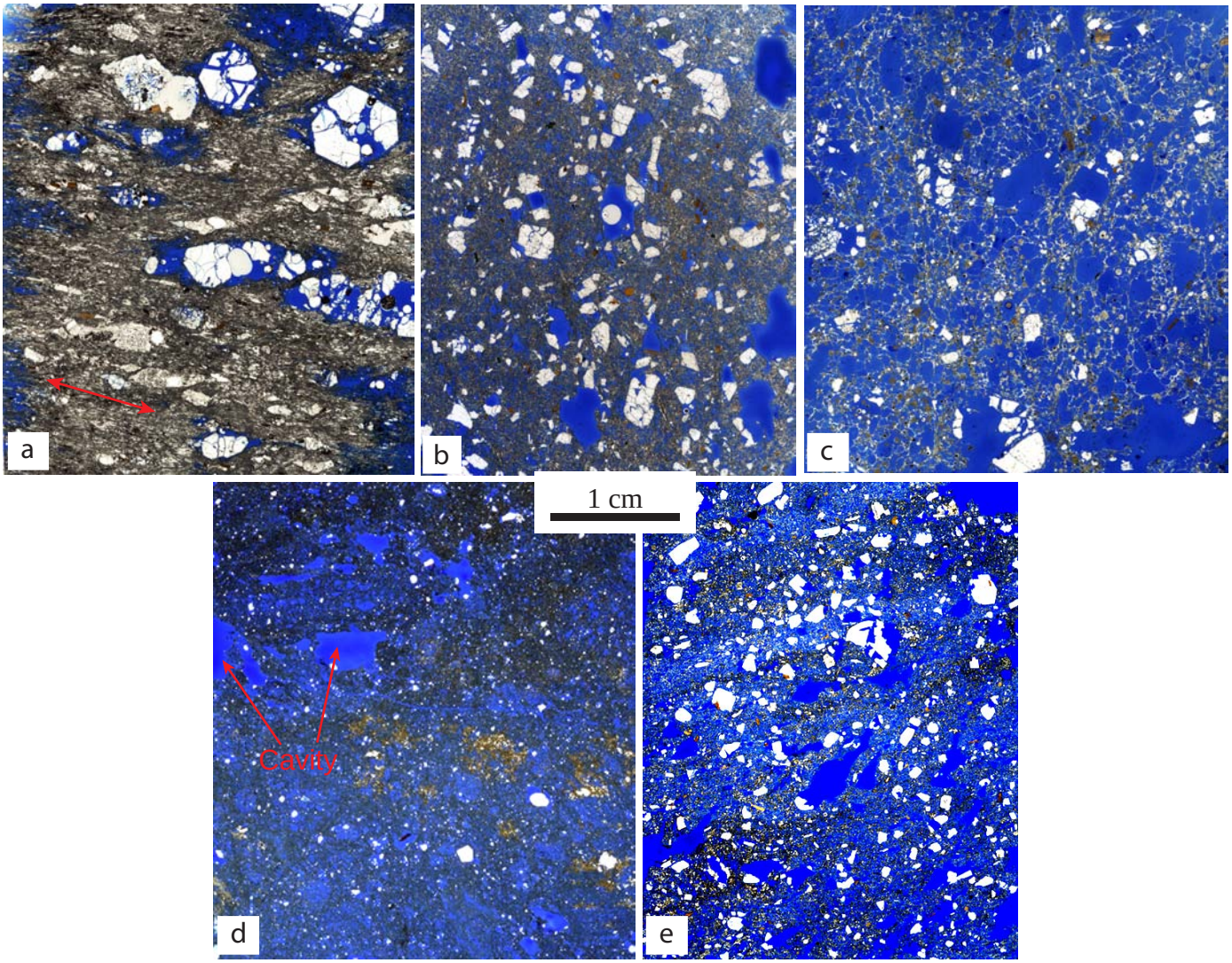

Figure 3

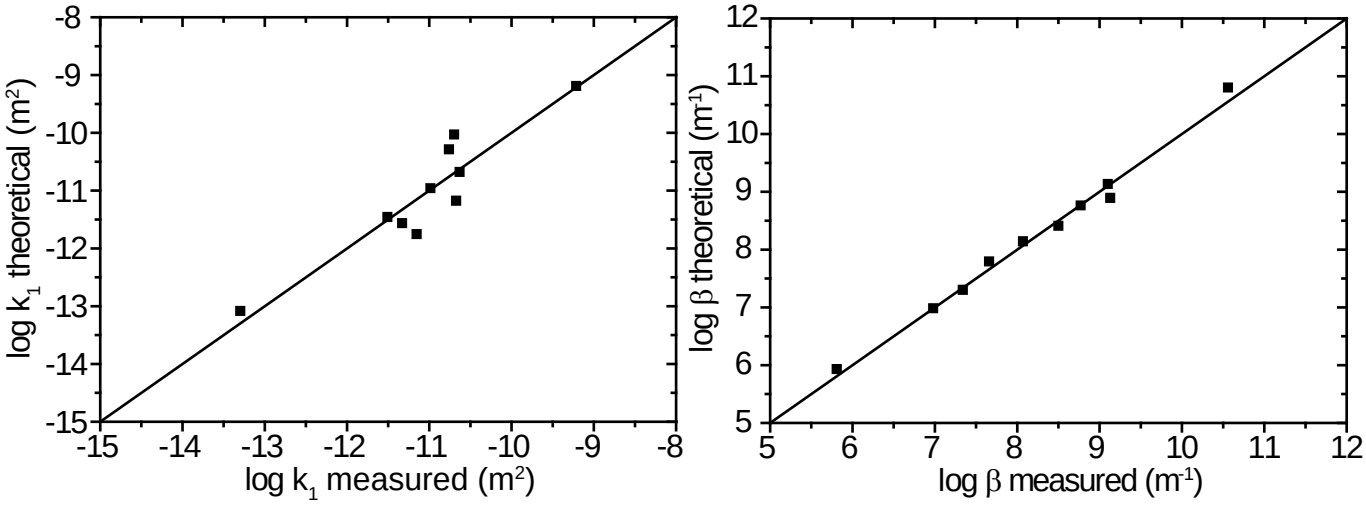
log k1 theoretical (m2)
log k1 measured (m2)
-8
-9
-10
-11
-12
-13
-14
-15
log β theoretical (m-1)
log β measured (m-1)
12
11
10
9
8
7
6
5

Figure 4

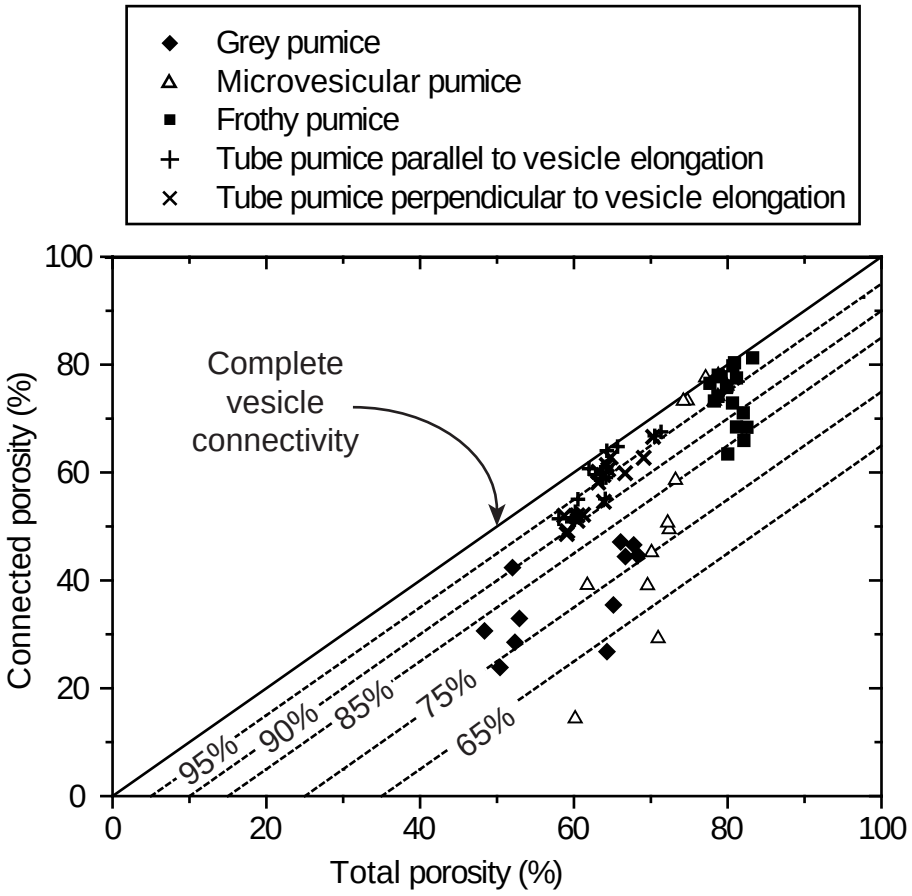
Grey pumice
Microvesicular pumice
Frothy pumice
Tube pumice parallel to vesicle elongation
Tube pumice perpendicular to vesicle elongation
Complete vesicle connectivity
95%
90%
85%
75%
65%
Connected porosity (%)
Total porosity (%)
0
20
40
60
80
100

Figure 5

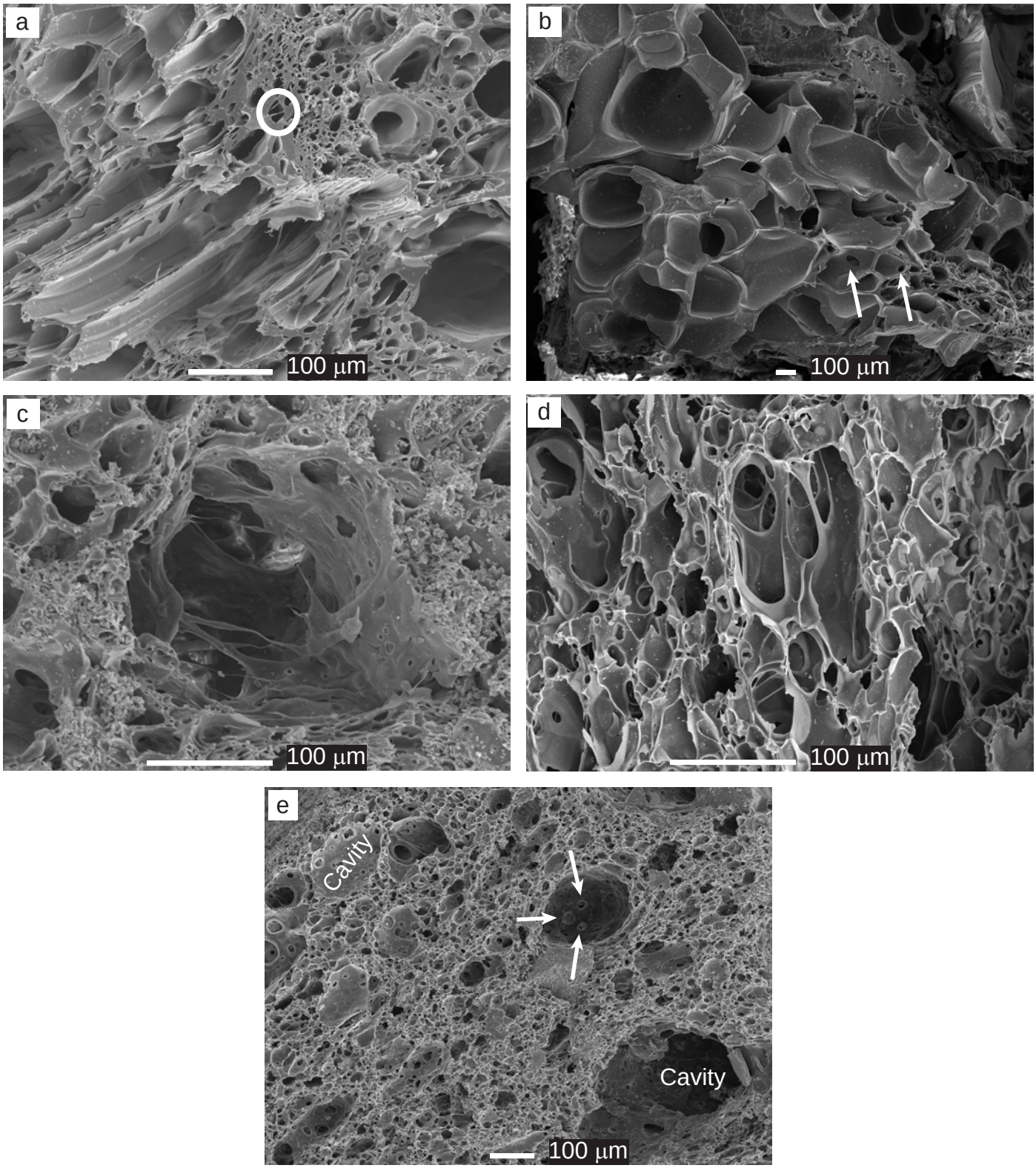

Figure 6

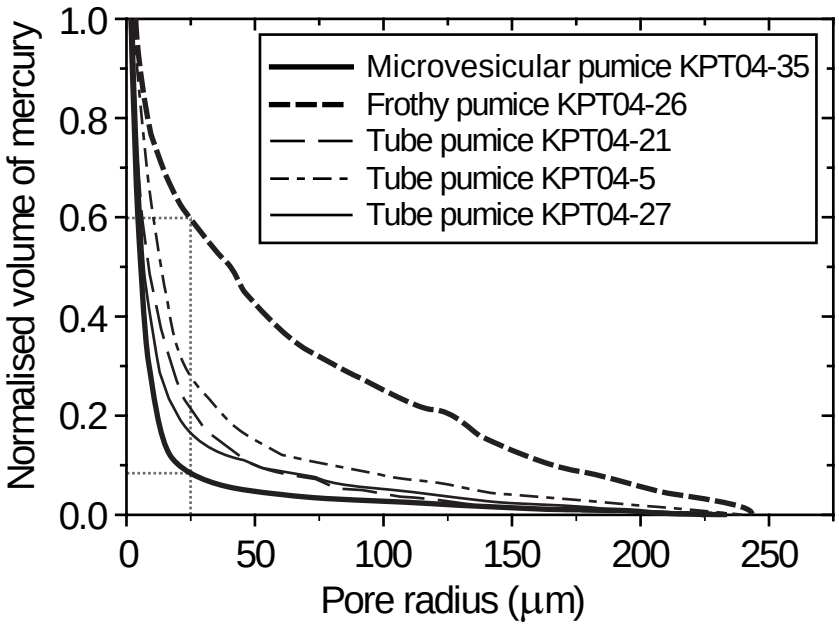
Normalised volume of mercury
1.0
0.8
0.6
0.4
0.2
0.0
0
50
100
150
200
250
Pore radius (μm)
Microvesicular pumice KPT04-35
Frothy pumice KPT04-26
Tube pumice KPT04-21
Tube pumice KPT04-5
Tube pumice KPT04-27

Figure 7

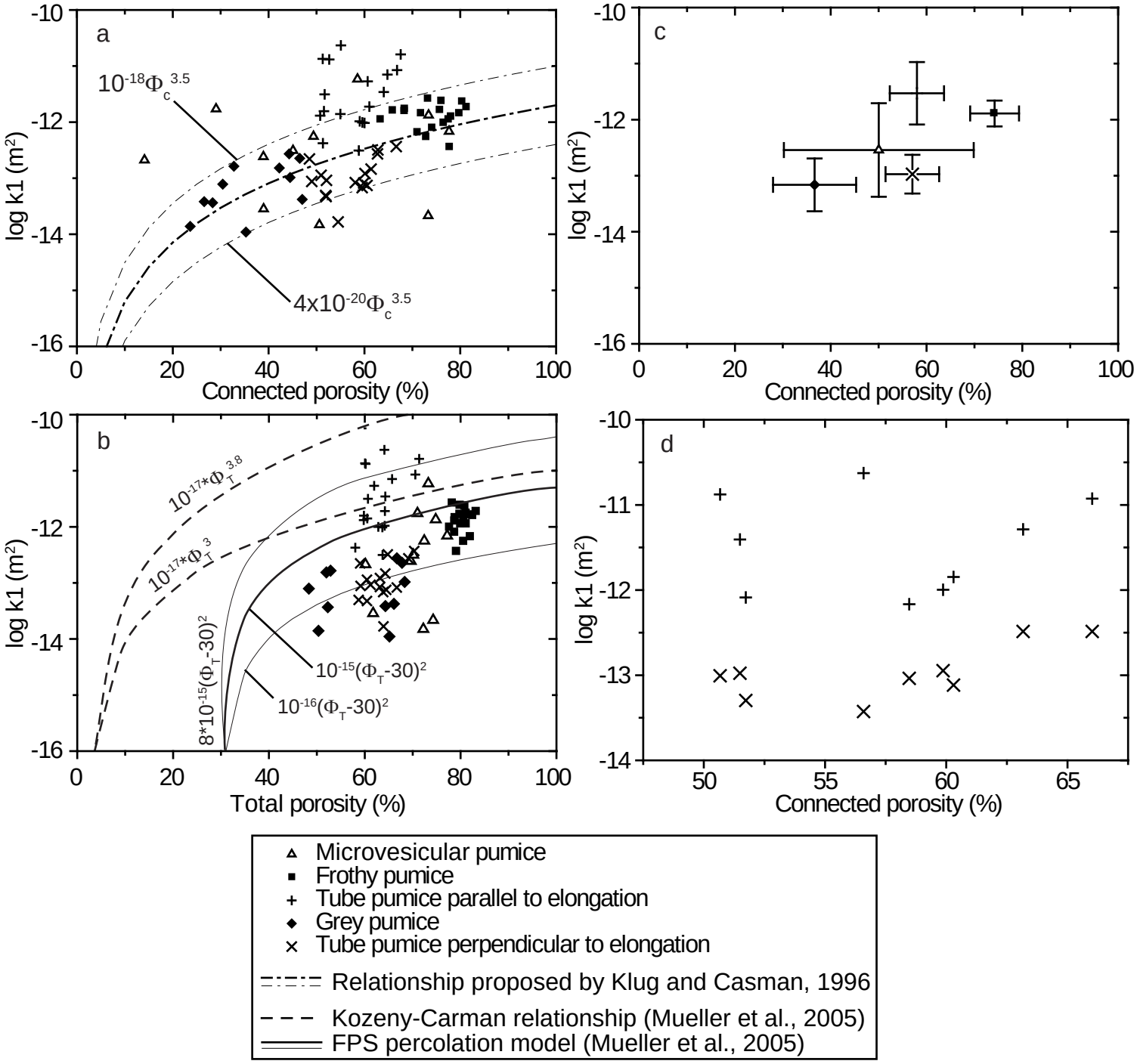
a
$10^{-18}\Phi_c^{3.5}$
$4x10^{-20}\Phi_c^{3.5}$
log k1 (m²)
Connected porosity (%)
c
b
$10^{-17}*\Phi_T^{3.8}$
$10^{-17}*\Phi_T^{3}$
$8*10^{-15}(\Phi_T-30)^2$
$10^{-15}(\Phi_T-30)^2$
$10^{-16}(\Phi_T-30)^2$
Total porosity (%)
d
Microvesicular pumice
Frothy pumice
Tube pumice parallel to elongation
Grey pumice
Tube pumice perpendicular to elongation
Relationship proposed by Klug and Casman, 1996
Kozeny-Carman relationship (Mueller et al., 2005)
FPS percolation model (Mueller et al., 2005)

Figure 8

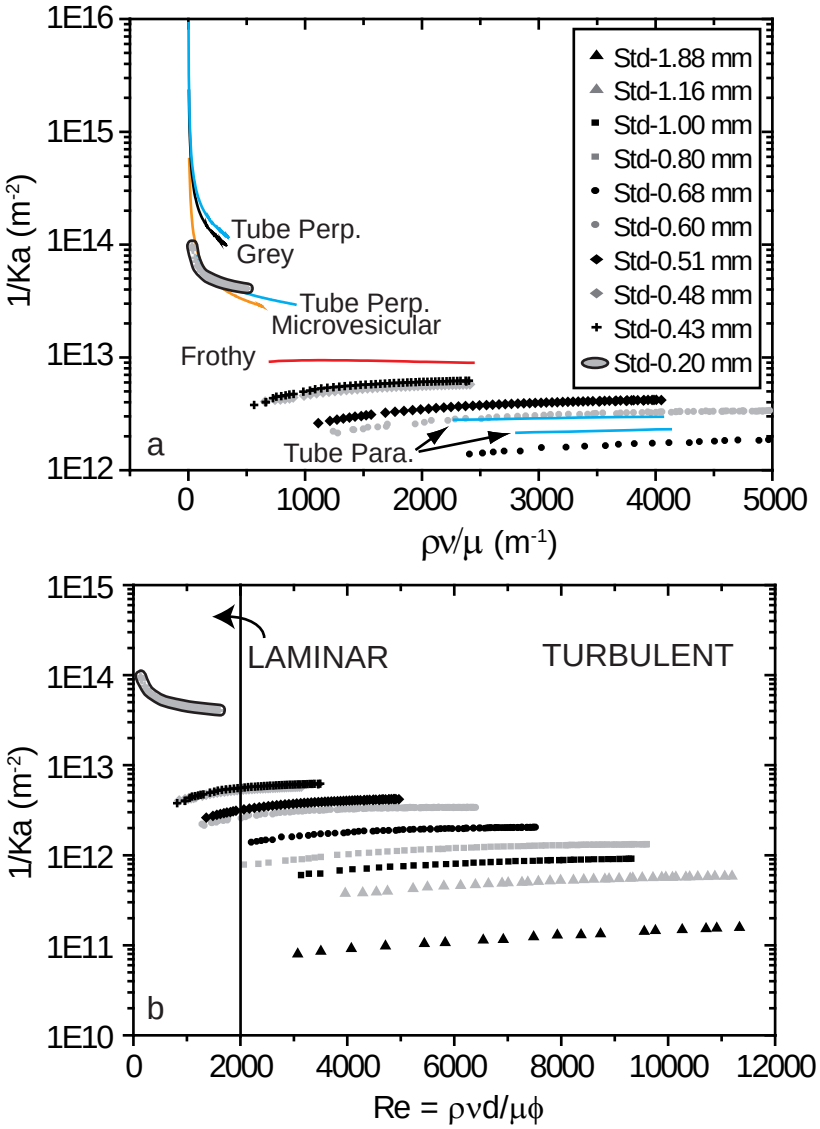
1E16
1E15
1E14
1E13
1E12
1/Ka (m-2)
Std-1.88 mm
Std-1.16 mm
Std-1.00 mm
Std-0.80 mm
Std-0.68 mm
Std-0.60 mm
Std-0.51 mm
Std-0.48 mm
Std-0.43 mm
Std-0.20 mm
Tube Perp.
Grey
Tube Perp.
Microvesicular
Frothy
Tube Para.
a
0
1000
2000
3000
4000
5000
ρν/μ (m-1)
1E15
1E14
1E13
1E12
1E11
1E10
1/Ka (m-2)
LAMINAR
TURBULENT
b
0
2000
4000
6000
8000
10000
12000
Re = ρνd/μϕ

Figure 9

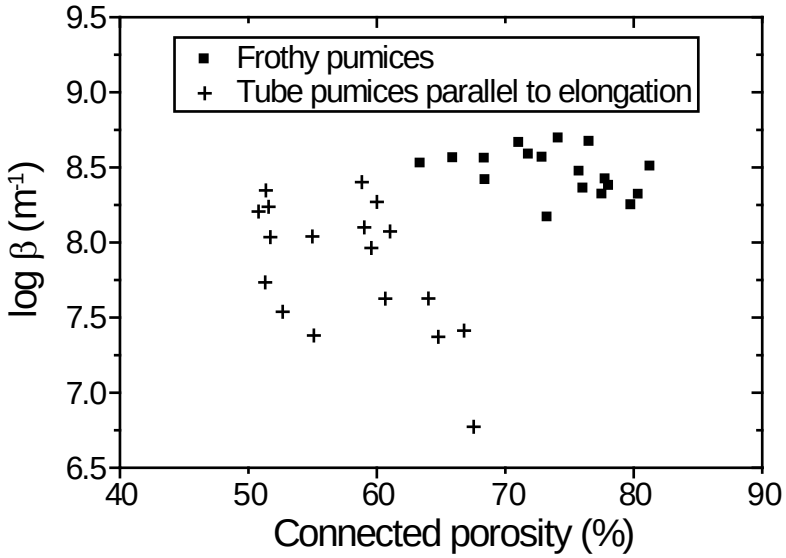
Frothy pumices
Tube pumices parallel to elongation
log β (m-1)
Connected porosity (%)
9.5
9.0
8.5
8.0
7.5
7.0
6.5
40
50
60
70
80
90

Figure 10

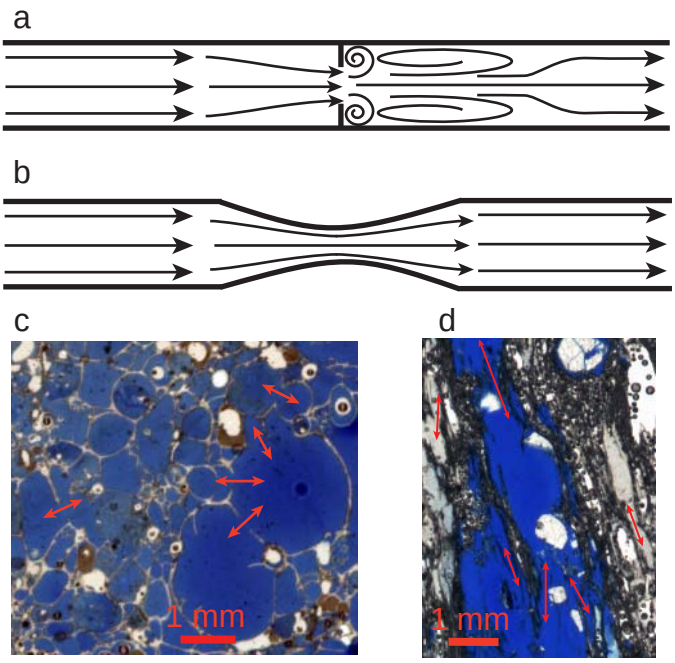

Figure 11

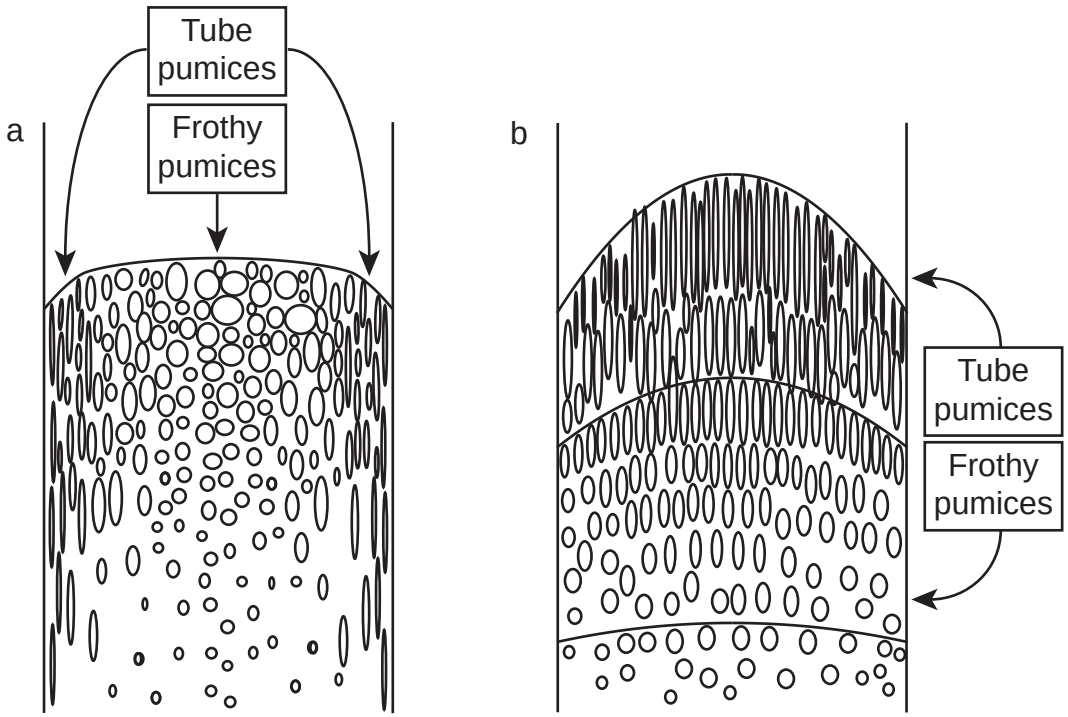
a
Tube pumices
Frothy pumices
b
Tube pumices
Frothy pumices

Figure 12